Experiments in Fluids (2021) 62:130
https://doi.org/10.1007/s00348-021-03224-5

RESEARCH ARTICLE

Exploring the capabilities of active grids

Lars Neuhaus[1] · **Frederik Berger**[1] · **Joachim Peinke**[1] · **Michael Hölling**[1]

Received: 25 November 2020 / Revised: 4 May 2021 / Accepted: 7 May 2021 / Published online: 27 May 2021

Abstract

Active grids are commonly used in wind tunnels to generate turbulence with different characteristic features. In contrast to the common objective to generate turbulence with a very high Reynolds number, this work focuses on a method of blockage induced flow design for the generation of special flow structures. Particularly, we aim to investigate the underlying constraints of this excitation method. For this purpose, the scale dependency of the excitation is studied by clearly defined structures such as periodic sinusoidal velocity variations, velocity steps, and single gusts. It is shown that the generation process is limited by the reduced frequency of the active grid motion. For low values of reduced frequencies the imprinted flow structures remain undamped, whereas for higher reduced frequencies they are damped. This insight leads to the constraint that the active grid motion needs to be modified to compensate for the underlying dynamic damping effects. Thus, the inserted energy has to be increased for the corresponding reduced frequencies. This finding can be transferred to the generation of turbulent flows, for which an exemplary adaption is shown .

Graphic abstract

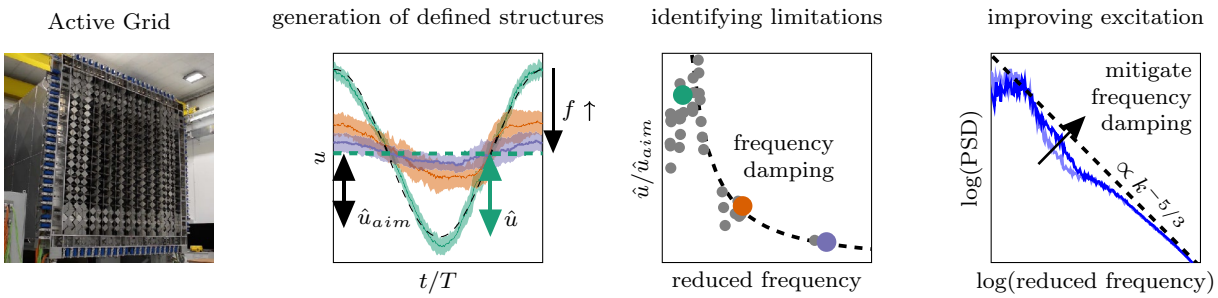

1 Introduction

For many engineering problems the impact of turbulence is of high relevance. Quite often, like for wind turbines, the environmental conditions are highly unsteady. Thus, for a deeper scientific investigation it is desirable to remodel this interaction of turbulence and objects under reproducible laboratory conditions.

The first approach to generate turbulent flows in a wind tunnel was made by applying a simple regular grid to the nozzle (Simmons and Salter 1934). Following this first grid experiment, different turbulence intensities and Taylor-scale Reynolds numbers were achieved by varying the grid mesh width, the tunnel cross sectional size, or the downstream position in the wind tunnel. For a long time such regular passive grids were the state of the art.

A new concept to generate turbulence was shown by Makita (1991), when he introduced an active grid. The change from passive to actively controlled grid elements allowed to generate a variety of new flow conditions and to increase the Reynolds numbers significantly. This was a big step, as high Reynolds numbers could now be generated also in smaller wind tunnels. Many new experiments

✉ Lars Neuhaus
lars.neuhaus@uol.de

Michael Hölling
michael.hoelling@uol.de

[1] Institute of Physics and ForWind, University of Oldenburg, 26129 Oldenburg, Germany

were initiated, which are summarized in a recent review by Mydlarski (2017). Alternating the excitation methods, grids are used (a) to generate homogeneous and isotropic turbulence (HIT) (see Mydlarski and Warhaft 1996, 1998; Shen and Warhaft 2000; Poorte and Biesheuvel 2002; Larssen and Devenport 2011; Hearst and Lavoie 2015; Griffin et al. 2019; Cekli et al. 2015), (b) to create a defined shear flow in the wind tunnel (see Cekli and van de Water 2010; Hearst and Ganapathisubramani 2017), and (c) to reproduce atmospheric wind conditions either directly (see Reinke et al. 2017; Kröger et al. 2018a) or by their statistical properties (see Knebel et al. 2011; Good and Warhaft 2011; Neuhaus et al. 2020).

The first active grid was operated in a synchronous mode, where all shafts are rotating with the same speed, but adjacent shafts in different directions. This allowed for an increase of the turbulence intensity. To further increase the turbulence intensity, a single-random asynchronous mode was introduced (Mydlarski and Warhaft 1996). In contrast to the synchronous mode, the direction of the rotation was changed individually for the shafts after random time steps. However, the constant rotational speed caused a peak in the velocity spectrum. To reduce this effect, Mydlarski and Warhaft (1998) modified this mode by slightly different rotational speeds for the different shafts. This peak in the spectrum was completely eliminated by the double-random asynchronous mode, in which the rotational speed (negative and positive speeds are possible) and the duration are chosen randomly and individually for each shaft (Poorte and Biesheuvel 2002). Hearst and Lavoie (2015) performed a comprehensive study of the initial conditions for active grid excitation and found that the highest homogeneity of the flow was generated by this double-random asynchronous mode.

All these methods focus exclusively on the movements of the active grid without direct reference to the resulting flows behind it. An alternative approach to this is a blockage induced flow design, which establishes a link between grid setting and generated flow. Therefore, the dependence of the wind velocity on the blockage (shaft angle) of the active grid is captured by a transfer function (see Knebel et al. 2011; Weitemeyer et al. 2013). Wind statistics were reproduced by randomly changing the global blockage of the grid according to the velocity distribution found in the atmosphere (see Knebel et al. 2011). Weitemeyer et al. (2013) introduced an operation of the active grid where they kept the global blockage constant, while changing the local blockage. This approach was further used for the direct reproduction of measured atmospheric wind by using a transfer function of the local blockage of the grid and the velocity behind it (see Reinke et al. 2017). It was also applied to mimic atmospheric wind statistics by using stochastic processes as input for the motion of the shafts (see Kröger et al. 2018b; Neuhaus et al. 2020).

Additionally, grids which increased the degree of freedom for the excitation were built. Hearst and Lavoie (2015) installed two active grids with staggered flaps. An even higher variability can be found for the grid by Bodenschatz et al. (2014), which allows to control all flaps individually. This grid allows for greater control of the spatial velocity correlations (Griffin et al. 2019).

Apart from classical turbulence generation and wind field reproduction, approaches have been made to generate special flow structures as defined in the IEC 61400-1 standard for wind energy (IEC 2019). One of these approaches with reduced complexity, uses a rotating bar, which blocks the wind while passing the wind tunnel cross section to generate inverse gusts (Neunaber and Braud 2020). Another approach is based on a fan array at the test section inlet, for which the fans can be controlled individually allowing to create shears and gusts on time scales as small as a few seconds (Shirzadeh et al. 2020). Gusts that are generated by applying the blockage induced flow design approach discussed in this paper were already used by Petrović et al. (2019) and Sinner et al. (2021).

In this paper, the scale-dependent influence of the dynamic variation of the active grid blockage on the flow is studied. Therefore, the blockage induced flow design approach is used for generating specific flow structures. In contrast to naturally decaying turbulence, flow structures can directly be imprinted on the corresponding scales by the active grid motion protocols. This work focuses on the exploration of the capabilities of active grids to excite the flow on different scales. By a dimensionless consideration it is shown, how the layout of an active grid results in limitations in the scales of the generated flow structures. This knowledge can further be transferred from specific flow structures to turbulence generation. Consequently, the paper is structured as follows. The experimental setup is presented (Sect. 2) and a method to tailor motion protocols (Sect. 3) by a transfer function of the active grid (Sect. 4) for different inflows is shown. Flow structures such as sinusoidal velocity variations, velocity steps, and single gusts are generated (Sect. 5) and the behavior of their limitations are discussed. The coherence of the flow is investigated in Sect. 6. The outcome of the investigation is further used to show a possible application to more complex turbulence time series (Sect. 7).

2 Experimental setup

The measurements are done in Oldenburg in a Göttingen type wind tunnel with a 3 x 3 m^2 cross section and a length of 30 m. The wind tunnel can be operated in an open (up to 32 m/s) or a closed (up to 42 m/s) test section configuration. Flow is generated by four fans with a power of 110 kW each and its temperature is kept constant by a cooling system with an effective cooling power of roughly 400 kW.

An active grid, 3 x 3 m^2, is mounted on the nozzle to manipulate the flow (Kröger et al. 2018a; ForWind 2021) (Fig. 1). The active grid has 80 individually controllable shafts, each equipped with rectangular flaps. The mesh width M is 0.143 m. The local blockage can be altered by changing the angle of the flaps. By this the global blockage can be varied from 21 to 92%.

The active grid is controlled by a real time system that moves the shafts according to predefined shaft angle time series. Further, the protocol allows to generate user defined trigger signals, which ensure a temporal matching of repetitions.

Two different hot-wire setups with single and triple 1-D hot-wire 55P16-probes by Dantec Dynamics are used for the measurements. The hot-wires are mounted on a 3 m high support in the vertical center of the wind tunnel. A distance of 4.6 m $\approx$ 32M downstream to the active grid was chosen as well as the open test section, see Fig. 1. One setup uses one single hot-wire on the centerline of the wind tunnel to characterize the flow structures (Sect. 5). The second setup with 3 hot-wires is used for the investigation of the coherence of the flow (Sect. 6). The hot-wire signals are sampled with a frequency of 20 kHz after being low pass filtered with 10 kHz.

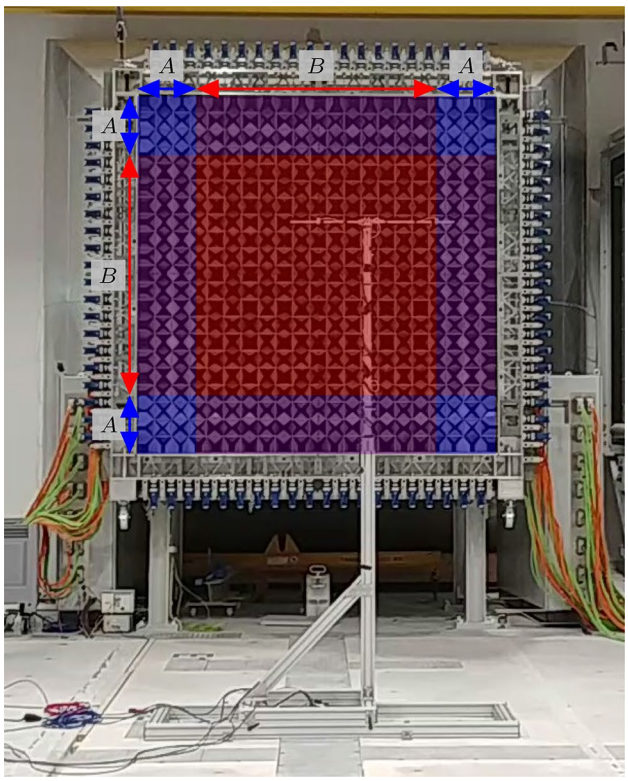

Fig. 1 Active grid and hot-wire support. Example of A-shaft group and B-shaft group combination for defined flow generation on a 2 x 2 m^2 square in the center

3 Shaft motion groups

The active grid motion protocols are designed to ensure an easy and secure operation. Furthermore we require that the flow must not be deflected and the global blockage of the active grid must remain constant.

To guarantee that no large redirection of the flow takes place, adjacent shafts are rotated in opposite directions, so that the flaps point in opposite directions. To keep the global blockage constant the active grid shafts are split in two groups, labeled with A and B (Fig. 1). For the first group (A) a shaft angle time series $\alpha(t)$ is prescribed. The second group (B) is following the shaft angle time series

$$\beta(t) = \arcsin\left((\sin(|\alpha(t)|) - 1 + x_{cb}) \cdot N_A/N_B\right), \quad (1)$$

which is given by the shaft angle time series $\alpha(t)$ and the corresponding number of shafts per group N_A and N_B ($N_B \geq N_A$). Due to this dependence (Eq. 1), the local blockage variations of both shaft groups compensate each other, so that the global blockage is approximately constant and can be set via the constant x_{cb}. In one group all shafts follow the same angle time series ($\alpha(t)$ or $\beta(t)$). However, adjacent shafts point in opposite directions (follow the angle time series with the opposite sign). In contrast to common excitation methods for the generation of high Reynolds number homogeneous isotropic turbulence (HIT), the shafts are not randomly rotating but flapping back and forth. The shaft angle is following a pre-defined time series (between $\alpha = 0°$ and $|\alpha| = 90°$) to dynamically change the local blockage (for a visual impression see ForWind (2021)).

Based on our approach, different combinations (patterns) of the two groups of shafts (A and B) can be picked. In this paper, we use a 2 x 2 m^2 square pattern in the center, as shown in Fig. 1. As mentioned before, the motion pattern for the active grid keeps the global blockage approximately constant, allowing to neglect pumping effects of the wind tunnel and to assume a constant load on the fans. At the same time special shaft dynamics allow to generate special temporal structures of the flow downstream. In particular, we use transfer functions to predict special temporal structures. This methodology will be outlined in detail in the following.

4 Transfer function

To allow for the generation of defined flow conditions, the dependence between wind velocity behind the active grid and shaft angle (corresponding to the blockage) needs to be determined. This relation between active grid and resulting flow is expressed by a transfer function, which we determine with the following procedure (see also Reinke et al. (2017)): For a constant wind tunnel fan speed (mean velocity) the

shaft angle α is varied from 0° to 90° with a low angular velocity of 1°/s (quasi-steady). The velocity $u(\alpha)$ is recorded at the position in the wind tunnel where later flow conditions should be created (here the centerline is used), as shown exemplarily in Fig. 2. From the measurements the transfer function u_{transfer} is extracted by a polynomial fit of 7th order for shaft angles α from 0° to 90°. The corresponding fluctuations are given by

$$u'(\alpha) = u(\alpha) - u_{\text{transfer}}(\alpha). \tag{2}$$

This procedure is repeated for different constant fan speeds u_{fan}. In this way a transfer function of

$$(\alpha, u_{\text{fan}}) \rightarrow (u_{\text{transfer}}(\alpha, u_{\text{fan}}), u'(\alpha, u_{\text{fan}})) \tag{3}$$

is obtained.

The transfer function (Eq. 3) allows to predict a velocity time series and its statistics (e.g. distribution, power spectra, and increment statistics) by a corresponding time series for the shaft angle $\alpha(t)$. Following the method introduced by Reinke et al. (2017), for every sample point of the grid motion (10–20 ms) the mean wind speed is extracted from the transfer function. Subsequently, a velocity time series with high temporal resolution (20 kHz) is created by a cubic spline interpolation between these sample points. To this velocity time series high frequency fluctuations are added, which consist of 10–20 ms of $u'(\alpha)$ for each sample point.

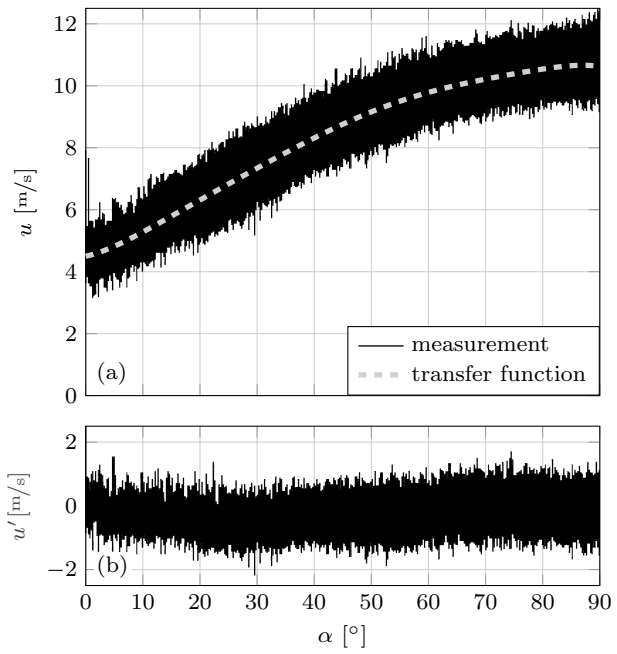

Fig. 2 Exemplary time resolved velocity measurement in dependence of the corresponding shaft angle α with extracted transfer function **a** and corresponding fluctuations u' **b** on the centerline behind the active grid

All this is also working vice versa. Having a velocity time series, the transfer function can be used to define the needed shaft angle time series $\alpha(t)$. This allows for tailored velocity time series.

A user-interface MATLAB-program was built to automatize the generation of active grid motion protocols including an automatized extraction of the transfer function of the active grid. This allows for an easy generation of new active grid motion protocols, tailored for the requested applications and inflows. In the next sections some examples are shown.

5 Generation of specific flow structures

Three different test cases are generated by the method just mentioned. The aim is to work out the range of validity of our method. First periodic sinusoidal velocity variations with different frequencies and amplitudes are studied. Subsequently, flow structures of upwards and downwards steps of the velocity are investigated. This step structure allows to see how symmetric the system behavior is. Finally gusts are studied, which provide information about the dependence of amplitude and symmetry on the frequency.

The corresponding motion protocols have to take into account the maximum rotational speed of the shafts and overshoots effects, which can be dampened by adjusting the acceleration and deceleration of the shaft motion. The single cases are repeated several times (sinusoidal velocity variation and gusts: 50 repetitions; velocity steps: 20 repetitions). The ensemble average of the centerline measurements are used for the detailed analysis.

5.1 Sinusoidal velocity variation

The first case of a sinusoidal velocity variation can be used to test objects under the influence of a simple periodic flow. To investigate the operation range of the active grid different frequencies and amplitudes are used.

Measurements are undertaken for six different frequencies from 0.5 to 10Hz and seven different aimed amplitudes $\hat{u}_{\text{aim}}$ from 0.5 to 3 m/s for mean wind speeds of 6 and 12 m/s with amplitudes from 1 to 6 m/s (Table. 1). The highest amplitudes are not investigated for the higher frequencies, as the loads for the active grid are too high for a secure operation.

In Fig. 3 the averaged velocity signals of three cases with the same aimed amplitude $\hat{u}_{\text{aim}}$ of 2.5 m/s and frequencies of 0.5, 2, and 4 Hz are shown. The solid lines correspond to the ensemble averages, the envelopes indicate its standard deviations, and the dashed black lines represent the corresponding sine fits of the ensemble averages.

For all frequencies a sinusoidal velocity variation can be recognized. The deviations from an ideal sine wave are

Table 1 Investigated sine frequency and amplitude combinations

$\overline{u}$ [m/s]	f [Hz]	$\hat{u}_{aim}$ [m/s]
6	0.5	0.5, 0.75, 1, 1.5, 2, 2.5, 3
	1	0.5, 0.75, 1, 1.5, 2, 2.5, 3
	2	0.5, 0.75, 1, 1.5, 2, 2.5, 3
	4	0.5, 0.75, 1, 1.5, 2, 2.5
	5	0.5, 0.75, 1, 1.5, 2
	10	0.5, 0.75, 1, 1.5, 2
12	0.5	1, 1.5, 2, 3, 4, 5, 6
	1	1, 1.5, 2, 3, 4
	2	1, 1.5, 2, 3, 4
	4	1, 1.5, 2, 3, 4
	5	1, 1.5, 2, 3, 4
	10	1, 1.5, 2, 3, 4

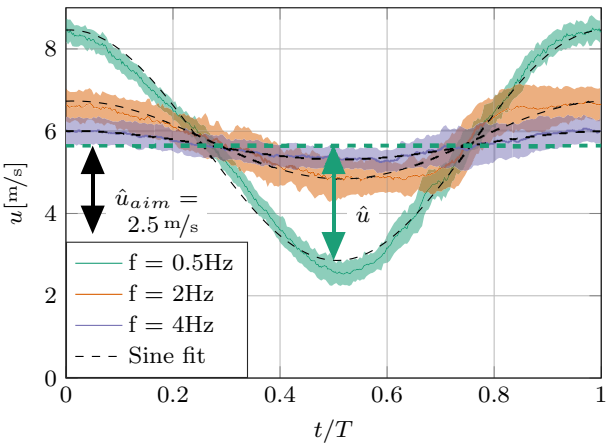

Fig. 3 Ensemble average, ensemble standard deviation (envelope), and sine fit of generated sinusoidal velocity variations for frequencies of 0.5, 2, and 4 Hz (corresponding to reduced frequencies k of 0.04, 0.15, and 0.31), with an aimed amplitude $\hat{u}_{\text{aim}}$ of 2.5 m/s

small. The relatively small standard deviation is quite constant over the period and indicates a good reproducibility. For the lowest frequency of 0.5 Hz the sinusoidal motion follows the expectations. For the higher frequencies the aimed amplitude of 2.5m/s is not reached.

To quantify the quality of the sinusoidal variation, we estimate the root mean square error (RMSE) between the measurement and the sine fit, which then is normalized by the estimated amplitude $\hat{u}$. The threshold for good quality is here the normalized RMSE of a flat line compared to a sine wave (RMSE $= \sqrt{0.5}$). The flat line corresponds to no signal, and signals with a larger RMSE than the one of no signal are considered as being of poor quality. Values below this threshold indicate a high quality sinusoidal velocity variation, whereas values above this threshold may not show a sinusoidal velocity fluctuation with the imprinted frequency or the imprinted flow may be dominated by noise (i.e. natural velocity fluctuations).

The dynamic response of the flow, and hence the quality of the sinusoidal velocity variation, seem to be connected to the overflow time of the flaps. This is one central finding of this work and discussed next.

The overflow time is commonly expressed by the reduced frequency

$$k = lf\pi/\overline{u}, \tag{4}$$

of the imprinted sinusoidal frequency f the diagonal of the flaps $l \approx 0.14$ m and the mean wind velocity $\overline{u}$. The resulting normalized RMSE is shown in dependence of this reduced frequency in a semi-log presentation (Fig. 4 (a)). The best results are found for low reduced frequencies and high amplitudes. With increasing reduced frequency, the normalized RMSE increases linearly in the semi-logarithmic presentation. The normalized RMSE of the lower amplitudes is consistently larger than the one of the high amplitudes. According to the introduced threshold of $\sqrt{0.5}$ (marked by a dashed line in Fig. 4 (a)) all cases of Fig. 3 show a good quality. Normalized RMSE of 0.16 for 0.5 Hz, 0.44 for 2 Hz, and 0.54 for 4 Hz are found, which is consistent with the visual impression, as for all cases the sinusoidal velocity variations can be recognized.

Besides the sinusoidal form, which is quantified by the normalized RMSE, the aimed amplitudes $\hat{u}_{\text{aim}}$ are compared with the measured ones $\hat{u}$ by the ratio of both amplitudes (Fig. 4 (b)). Sinusoidal velocity variations with poor quality are marked by an X-symbol. The dependence of this amplitude ratio can be divided into three regions. Up to approximately $k = 0.075$ the aimed amplitude can be achieved. In the second region for $0.075 < k < 0.2$, the amplitude is damped to 20– 50% of the aimed amplitude. For larger reduced frequencies ($k > 0.2$), the amplitude is strongly damped to less than 20% up to cases where hardly any sinusoidal motion can be detected. Together with the RMSE results these regions can be linked to the different states of the flow described, namely, quasi-steady state ($k \leq 0.05$), unsteady state ($k > 0.05$), and highly unsteady state ($k > 0.2$). Further, the reduced frequency region with a low damping of the amplitude also corresponds to the region with a good quality (Fig. 4 (a)).

For $k \geq 0.075$ it is found that the amplitudes decay with a power law $\hat{u}/\hat{u}_{\text{aim}} = 0.025k^{-1.4}$. To verify this result, a second measurement with twice the mean wind speed ($\overline{u} = 12$ m/s) was done (Tab. 1). All results of this measurement fit well to the former results with lower wind speed.

In general, it can be recognized, that for the quasi-steady state and up to $k = 0.075$ the transfer function (Sec. 4) can be used to directly design the flow. For higher reduced frequencies the imprintable amplitude is lower than expected

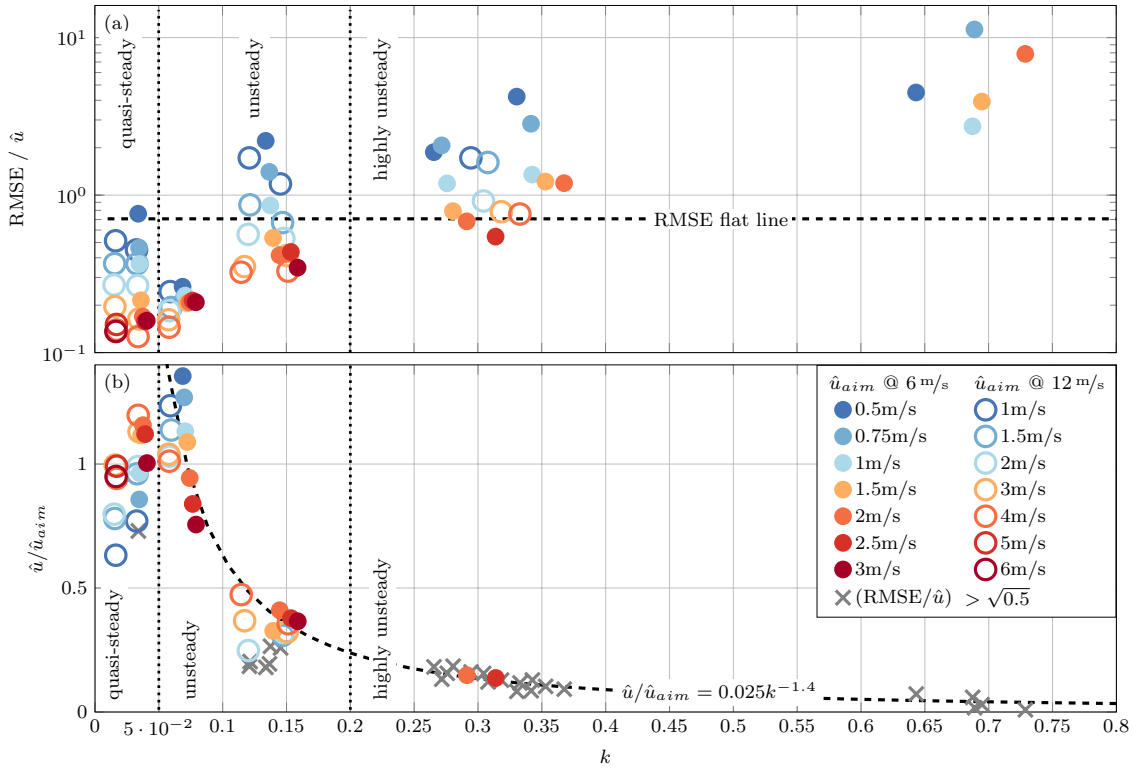

Fig. 4 Root mean square error (RMSE) normalized by the measured amplitude (**a**) and amplitude ratio (**b**) in dependence of the reduced frequency k

from the transfer function. Hence, the quasi-steady transfer function needs to be adapted for dynamic effects to compensate the damping of the amplitude for reduced frequencies $k > 0.075$ and may not be applicable for very high reduced frequencies of $k > 0.3$ (Sect. 7).

5.2 Velocity step

To further understand the dynamics of flow excitations, the active grid is used to generate jumps between two flow conditions. Again the aim is to determine the limits of producible velocity steps with the active grid and to study steps with different amplitudes. We distinguish between a velocity increase and decrease and differences in the dynamic response of the flow are investigated.

Measurements are undertaken for nine different step amplitudes from 0.5 to 6 m/s and a lower wind speed level of 5 m/s. Fig. 5 shows the ensemble average of the smoothed and downsampled 20 repetitions (solid line) and its standard deviations (envelope).

Velocity step amplitudes up to roughly 6 m/s are possible and are well reproduced. For the small step amplitudes ($\leq$ 2.5 m/s) fluctuations (damped oscillations) after the upwards and downwards steps can be recognized. An asymmetric behaviour is found for larger steps amplitudes. Here large fluctuations (damped oscillations) are found after the downwards step, whereas hardly any fluctuation can be recognized after the upwards step.

To quantify the steps, the velocity increments $\mathrm{d}u = u(t + \mathrm{d}t) - u(t)$ for different temporal increments $\mathrm{d}t$ are determined. Per temporal increment the maximum (upwards step) and minimum (downwards step) velocity increment is determined. Fig. 6 shows the temporal increment $\mathrm{d}t$ after which the absolute value of the maximum/minimum velocity increment exceeds 80 and 90% of the aimed step amplitude $\mathrm{d}u_{\mathrm{aim}}$. This is giving a rough measure of the time needed to complete the steps of different amplitudes.

For the upwards step it is found, that larger step amplitudes need longer time to reach the aimed value. Step amplitudes below 3 m/s need less than 0.5 s to reach 90% of the aimed value. The largest step amplitude takes roughly 0.75 s to reach 90% of the aimed value.

For the downward step the opposite dependence can be found. Steps above 1 m/s are completed to 90% after roughly 0.5 s. Smaller step amplitudes take way longer and up to 0.9 s.

To summarize the step measurements, it can be seen that it is possible to create different velocity steps with the active

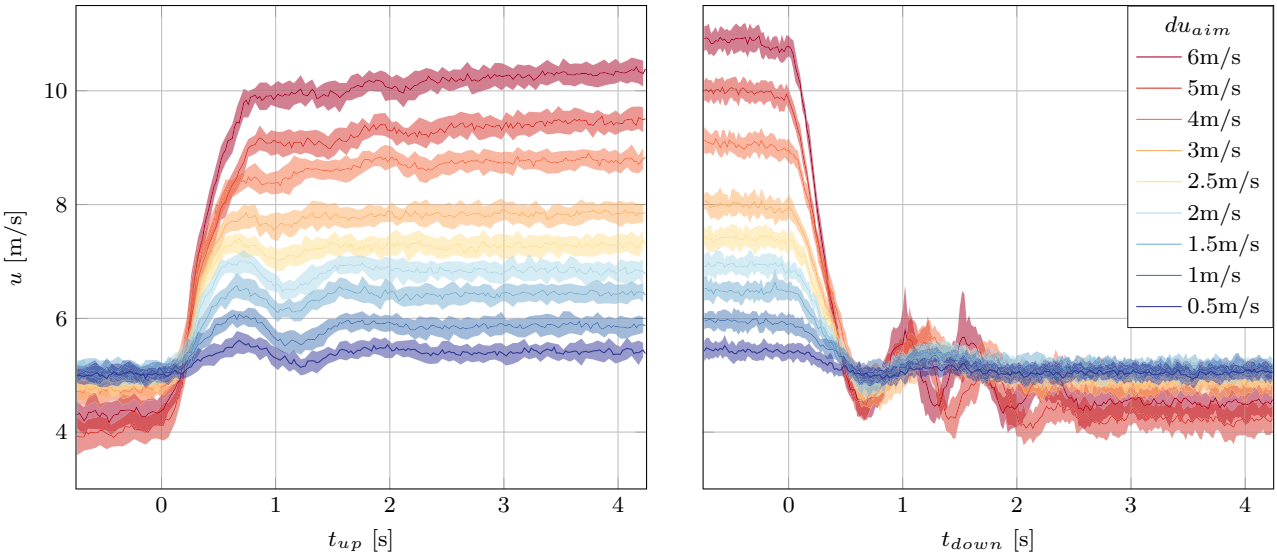

Fig. 5 Smoothed and downsampled ensemble average (solid lines) and its standard deviation (envelope) of the velocity steps generated by the active grid

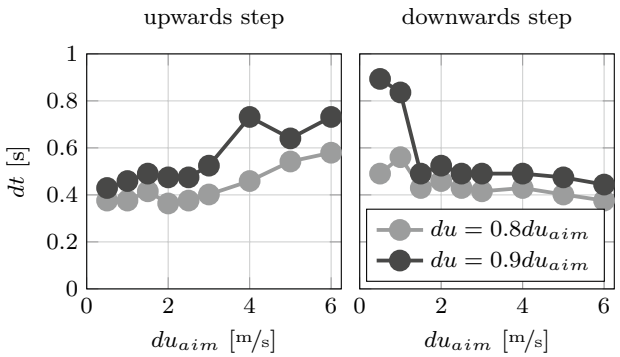

Fig. 6 Time increments dt to reach 80 and 90% of the aimed step amplitude du_{aim} in dependence of the aimed step amplitude du_{aim} for upwards and downwards steps

grid. Very fast and large velocity steps up to 6 m/s within 0.75 s can be generated.

Fluctuations of the velocity after an upwards or downwards step may occur. For very large step amplitudes a slight drift of the velocity and a lower wind speed of the lower level was observed, which may be caused by the rapid change of the local blockage to which the whole wind tunnel has to adapt (Fig. 5). Interestingly, the time for the completion of the step depends not only on the step amplitude, but also on the sign of the step. Large steps are completed faster for a velocity decrease, whereas small step amplitudes are completed faster for a velocity increase. This shows some asymmetry between the dynamic response of the flow and the velocity manipulation by the active grid.

5.3 Gust

Here we investigate gusts as a third flow structure and use the IEC-standard 61400-1 (IEC 2019). The standard originates from the field of wind energy and it is used to define test cases for wind turbine design. Different amplitudes and duration are tested for the gust.

The equation for the temporal change of a gust

$$u = u_0 - 0.37u_{\mathrm{gust}} \sin\left(\frac{3\pi t}{2T_{\mathrm{peak}}}\right)\left(1 - \cos\left(\frac{2\pi t}{2T_{peak}}\right)\right) \quad (5)$$

is given by the IEC-standard with the mean wind speed u_0 the gust magnitude u_{gust} and the gust peak duration T_{peak}. However, for wind tunnel experiments a scaling needs to be considered, leading to reduced T_{peak} and velocity, depending on the application. These parameters are used as an input for the active grid. Four peak durations from 0.25 s to 2 s and four different gust magnitudes u_{gust} from 2 to 5 m/s are tested for a mean wind speed u_0 of 6.25 m/s.

Four exemplary measurements are shown in Fig. 7 with the same aimed gust magnitude $u_{\mathrm{gust,aim}} = 4$ m/s and with different peak duration of $T_{\mathrm{peak,aim}}$, from 0.25 s to 2 s. The dashed line indicates an ideal gust (Eq. 5). It can be seen, that the measured peak magnitude u_{gust} gets damped for shorter aimed peak duration $T_{\mathrm{peak,aim}}$. For $T_{\mathrm{peak,aim}} \leq 0.5$ s, the measured peak duration T_{peak} gets longer than $T_{\mathrm{peak,aim}}$. In particular, the decreasing part with a second dip occurs delayed compared to the expectation after Eq. 5. For longer aimed peak duration ($T_{\mathrm{peak,aim}} \geq 1$ s) the gust shapes are close to the one expected.

To quantify the individual cases, the peak duration T_{peak} and the gust magnitude u_{gust} are estimated from the measurements according to Fig. 7. The peak duration T_{peak} is determined by the time difference between the two dips. The gust magnitude $u_{\text{gust}} = (u_{\text{gust},1} + u_{\text{gust},2})/2$ is estimated by the mean of the velocity difference between first dip and peak $u_{gust,1}$ and second dip and peak $u_{gust,2}$.

These characterising quantities are studied in dependence of the inverse of the aimed peak duration $\frac{1}{T_{\text{peak,aim}}}$, which is proportional to the reduced frequency (Eq. 4), but can not be explicitly defined due to the superposition of different frequencies.

Figure 8a shows which duration T_{peak} can be achieved. A saturation at a peak duration of $T_{\text{peak}} = 0.8$ s is found. Shorter peak durations can not be obtained with our active grid and T_{peak} starts to increase for faster excitations.

In Fig. 8b it is shown how the gust magnitude gets damped, which is in accordance with the observation for the sinusoidal velocity variation. For the shortest aimed peak duration a comparable damping as in the unsteady state region can be observed. Besides this qualitative result, a direct quantitative comparison is not possible.

Additionally to the amplitude and the duration of the gust, the symmetry of the gust is influenced if the aimed peak duration becomes shorter. To quantify the symmetry of the gust we determine the correlation of the right side and the left side of the gust (Fig. 8c). Here we take the maximum of the measured signal to define left and right side. For low inverse aimed peak duration ($\frac{1}{T_{\text{peak,aim}}} \leq 1$ 1/s) high correlations (> 80%) are found. The correlation is reduced for higher inverse aimed peak duration. For the highest inverse aimed peak duration, the correlation is strongly reduced to values below 50% and only for the

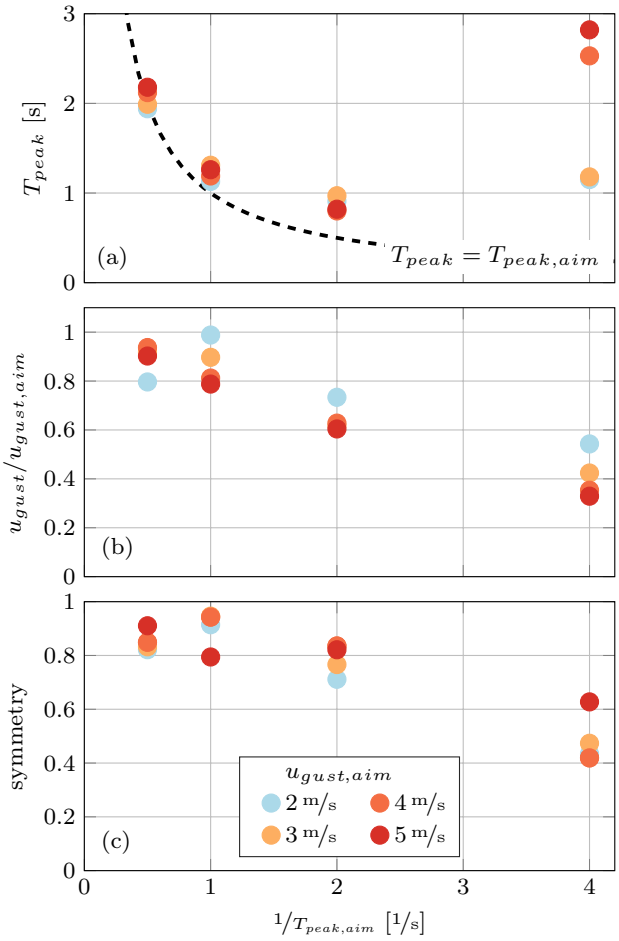

Fig. 8 Measured peak duration T_{peak} (**a**), normalized measured gust magnitudes $u_{\text{gust}}/u_{\text{gust,aim}}$ (**b**), and correlation of left and right side of the peak (symmetry) (**c**) in dependence of the inverse aimed peak duration $\frac{1}{T_{\text{peak,6}}}$

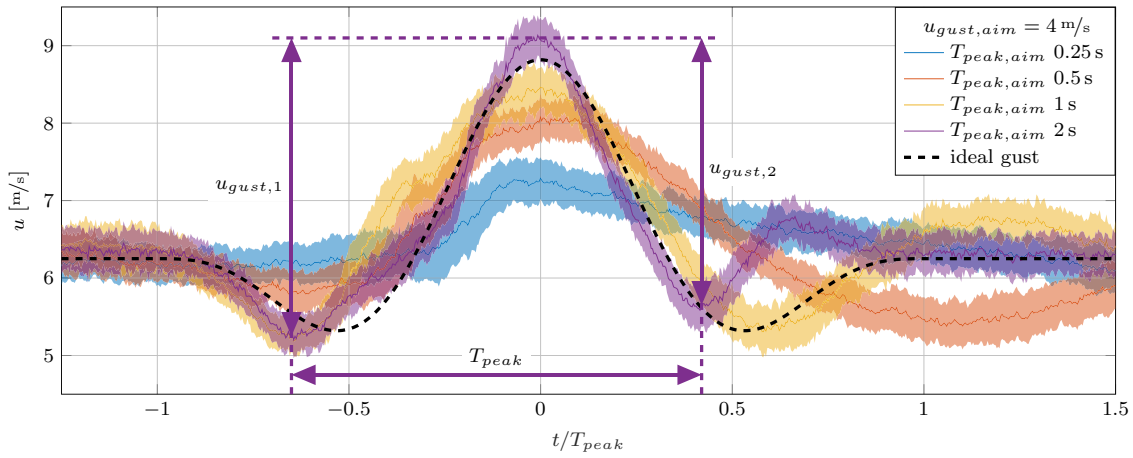

Fig. 7 Ensemble average (solid lines) and its standard deviation (envelope) of gusts generated by the active grid with aimed duration from $T_{\text{peak,aim}} = 0.25$ s to 2 s compared to an ideal gust (Eq. 5). For a better visualization, the gust peak is shifted to $t = 0$

largest gust magnitude the correlation is found at roughly 65%.

To conclude the gust investigations, we see that high magnitudes up to $u_{gust} = 5$ m/s were achieved. The shortest peak duration was found to be in the order of $T_{\text{peak}} = 0.8$ s. This is in good agreement with the findings from the velocity step, where steps (corresponding to half a gust peak) were successfully generated on comparable time scales (Sect. 5.2).

For aimed peak duration of $T_{\text{peak,aim}} \geq 0.5$ s well-shaped gusts with symmetry correlations above 70% can be created. The gusts are repeated with some temporal spacing between each other. Hence, the flow has time to adapt to the undisturbed case (in contrast to the sinusoidal velocity variation). This revealed an increasing asymmetric response of the flow for decreasing aimed peak duration. For short aimed peak duration ($T_{\text{peak,aim}} \leq 0.5$ s), the gusts exhibit longer peak duration than aimed for. However, it is possible to create comparatively short and strong gusts, which are close to the shape defined by the IEC-standard.

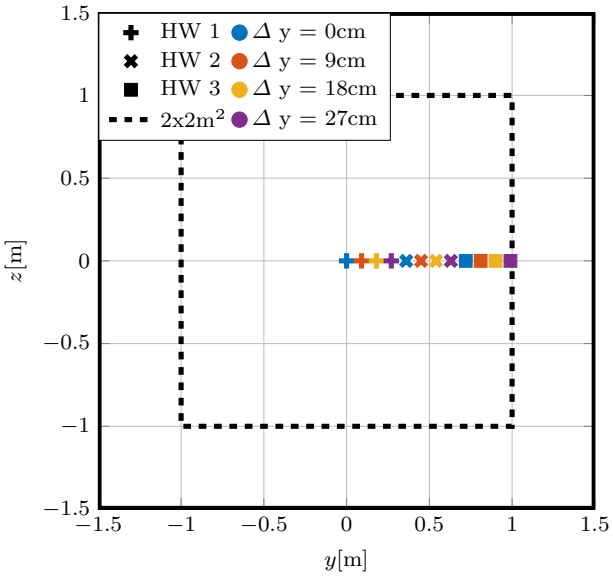

Fig. 9 Positions of hot-wires for coherence measurements

6 Coherence

The different generated flows were characterized by one single point measurement on the centerline of the tunnel. For an application it is important to ensure a similar flow behavior on a certain cross section.

To study the coherence of the generated flows, multiple transversal shifted positions are investigated. In total 12 hot-wire positions are considered ranging from the centerline to a transversal shifted position of 0.99 m with a spacing of 0.09 m. Thereto, three hot-wire probes are used with a transversal spacing of 36 cm, which are shifted collectively (Fig. 9). Here a fully symmetric flow over the cross section is assumed, as the active grid and the active grid motion are symmetric to the center point. Hence, the transversal shift by roughly 1 m should give a valid approximation of the coherence of the flow in a cross section of the size of 2 x 2 m^2.

For the different single events a few representative cases are measured for all 12 positions. Frequencies of 0.5 Hz with 3 m/s, 1 Hz with an amplitude of 0.5 m/s and 2 Hz with 3 m/s are investigated for the sinusoidal velocity variation. Large and small velocity steps (1 and 6 m/s) upwards and downwards are considered. For the gusts, peak durations of 0.5, 1, and 2 s with a gust magnitude of 5 m/s for the shortest duration and 4 m/s for the two longer durations are investigated. The correlations

$$\rho(y) = \frac{\sum u'(t,y)u'(t,y=0)}{\sqrt{\sum \left(u'(t,y)\right)^2 \sum \left(u'(t,y=0)\right)^2}} \tag{6}$$

of the ensemble average of the different positions ($u'(t,y) = u(t,y) - \overline{u}(y)$) with the ensemble average of the centerline ($u'(t,y=0) = u(t,y=0) - \overline{u}(y=0)$) are determined for all representative cases (Fig. 10).

The correlations in the center region ($y \leq 0.63$ m) are very high (> 0.91). For the positions farther outside ($y \geq 0.72$ m) the correlations are reduced. The correlation for the outer position ($y = 0.99$ m) is found to be still above 0.5 for most cases. For some cases correlations up to 0.8 can be found for the outer measured position. The lowest correlations are found for fast and high velocity variations (StepDown 6 m/s and Sine 2 Hz). For slow variations the highest correlations are found (Sine 0.5 Hz).

The presented method allows for the generation of flow structures with a good coherence on a large area corresponding to the region of one shaft motion group. Only measurements at the outer positions show lower correlations, which is to be expected as they are located in the shear layer between the different shaft motion groups. On a large cross section (1.25 x 1.25 m^2) very high correlations (≥ 0.9) can be found. Preliminary investigations on the downstream development of a single gust on the centerline showed a robust behavior of the structures over several meters in the stream-wise direction (see supplemental material).

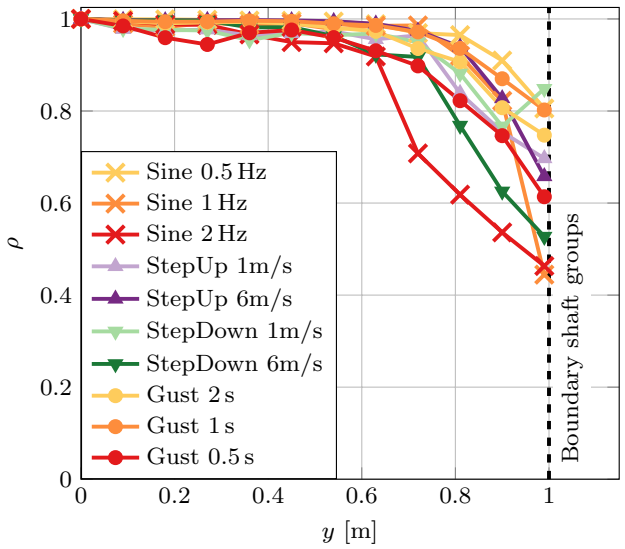

Fig. 10 Correlation of the ensemble average of different generated flows measured at transversal shifted positions with the corresponding measurement at the centerline

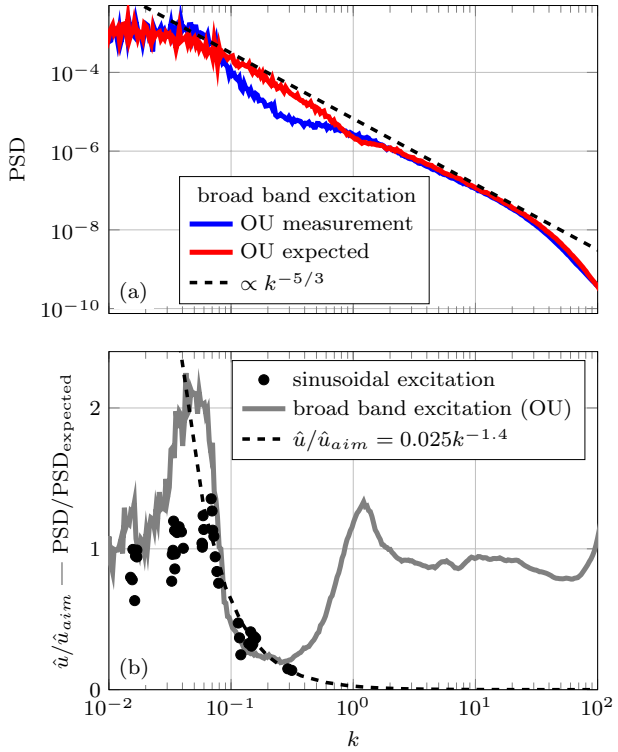

Fig. 11 Expected and measured power spectral density (PSD) for the broad band excitation (Ornstein–Uhlenbeck (OU)) **a** and normalized PSD and results from sinusoidal inflow (Fig. 4 b) **b** in dependency of the reduced frequency k

7 Application to turbulence

A clear dependence of the excitable frequencies on the reduced frequency was found. The amplitude damping, which occurs for high reduced frequencies, needs to be considered in the generation process.

Besides the investigation of specific frequencies and a superposition of different frequencies (gust) also the effect of a broad band excitation is of interest. The findings from the sinusoidal velocity variation are applied to the generation of fully developed turbulence in the wind tunnel by an active grid. The goal is to generate a flow that satisfies the $-5/3$ power law of Kolmogorov (1941) over a wide range directly through the motion protocol of the active grid. Therefore, a 10 min turbulent time series is generated by a broad band excitation based on a stochastic process exhibiting a power law decay (Ornstein–Uhlenbeck process (OU)) as presented by Neuhaus et al. (2020). By the quasi-steady transfer function (Sect. 4) the expected velocity time series and the corresponding expected spectra are determined. This expected spectrum (red curve) and the measured spectrum (blue curve) in dependence of the reduced frequency are shown in Fig. 11a in a double logarithmic presentation.

Three regions can be identified in the power spectra. In the first region for reduced frequencies up to $k \leq 0.075$, the measured power spectra behaves as expected and follows the $-5/3$ power law. From $k = 0.075$ to $k = 0.7$, a deviation from the power law and the expected power spectra can be observed. Hence, the active grid motion based on the Ornstein–Uhlenbeck process is not exciting the flow in the expected way, as already observed for the sinusoidal velocity variation (Sect. 5.1). For higher reduced frequencies ($k \geq 0.7$), the measured power matches the expected one again. This is caused by the different excitation of the flow for these frequencies, as the fluctuations are excited by the grid flap design and not by an active motion of the shafts. Hence, even the active excitation of complex flows is damped in the same region ($k > 0.075$) as shown for the simple sinusoidal inflow cases.

The quotient of the measured spectrum to the expected one (OU excitation) is shown in Fig. 11b in a semi-logarithmic presentation. It can be recognized, that the measured spectra (gray line) gets damped not only in the same region but in the same way as the amplitudes of the sinusoidal inflow (markers and dashed line from Fig. 4b) get damped. This comparability helps to understand the excitation by the active grid and the dynamic response of the flow to its motion.

To overcome this limitation, a first simple approach is shown exemplarily for the broad band excitation. Therefore, a stochastic process without a power law decay in the damping region (white noise (WN)) is used for the active grid motion. Using the quasi-steady transfer function the white noise expected spectrum (red curve) is determined (Fig. 12). In contrast to the previously shown broad band excitation

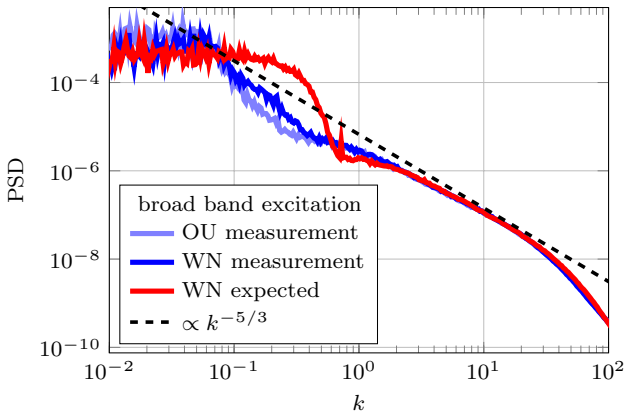

Fig. 12 Expected and measured power spectral density (PSD) for the adapted broad band excitation (white noise (WN)) in dependency of the reduced frequency k in comparison to the unadapted broad band excitation (Ornstein–Uhlenbeck (OU))

Table 2 Statistics of turbulent time series generated with a broadband excitation based on an Ornstein–Uhlenbeck process (OU) and white noise (WN)

Name	$\langle u \rangle$ [m/s]	$\sigma(u)$ [m/s]	skewness	flatness
OU	7.35	0.98	−0.25	3.01
WN	7.29	0.86	−0.23	2.93

(OU) (Fig. 11, red curve) the expected energy in the region $0.075 \leq k \leq 0.3$ is increased. The measured spectra of the flow generated by this adapted broad band excitation (WN) contains more energy in the region, where strong damping was observed for the unadapted broad band excitation (OU). In comparison to the unadapted broad band excitation (OU), the WN spectra is closer to the $-5/3$ power law. At the same time, the statistics of the generated velocity time series are hardly affected by this adaption (Tab. 2). This is just a first simple improvement, but it shows the capability of this adaption to handle dynamic effects and tailor active grid motion protocols to its applications.

However, still some lack of energy can be observed. Undergoing some transition further downstream will allow the flow to adapt to a fully developed turbulence (see Neuhaus et al. (2020)). By this adaption it may be possible to further control the position of this transition. Also the generation of comparable flow conditions in a larger longitudinal region could be possible by an active variation of the introduced energy on the different scales.

8 Conclusion

In this study on the possibilities to generate temporal flow structures with an active grid, a dependence of the excitable frequencies on the reduced frequency was found for the sinusoidal velocity variation. An asymmetric temporal behavior was found for velocity steps and gusts, which in combination with fluctuations after such single events showed the necessity to distinguish between positive and negative velocity increments, as the flow adapts differently to those flow manipulations.

Using a quasi-steady transfer function of the active grid allows to generate flow structures with low reduced frequencies. For reduced frequencies $k > 0.075$ a damping of the amplitudes is observed. Additionally, the quality of flow structures decreases, but is found to be good for high amplitudes as long as the reduced frequency k is below 0.3. However, with increasing reduced frequency the shape deviates further from the expectations.

Furthermore, the same dependence on the reduced frequency is found for turbulence generating protocols. The energy introduced at high reduced frequencies $k > 0.075$ by the active grid is below the expectations from the quasi-steady transfer function. Adjusting the active grid motion protocols allows to increase the energy in the damped region and to bring the spectra closer to the desired $-5/3$ power law. Thus, the dependence on the reduced frequency is not limited to specific flow structures, but can be found for a variety of flows with different complexity.

The dimensionless characterisation of the capabilities of the active grid allows to apply these results to other grids. In preliminary investigations we found a comparable behavior in three different sized wind tunnels (cross sections: 3 x 3 m^2, 1 x 0.8 m^2, and 0.25 x 0.25m^2) equipped with active grids (flap diagonals: 0.14, 0.106, and 0.049 m). Hence, we propose to use the worked out limitation as design parameter for active grids.

Supplementary file1 (DOCX 104 kb)Supplementary Information The online version contains supplementary material available at https://doi.org/10.1007/s00348-021-03224-5.

Acknowledgements We thank the Federal Ministry for Economic Affairs and Energy of Germany (BMWi) + MWK Lower Saxony, DFG (Grossgeraet) for funding parts of this work. Furthermore, we thank Lars Kröger, David Onnen, Lisa Rademacher, and Piyush Singh for fruitful discussions.

Funding Open Access funding enabled and organized by Projekt DEAL.

References

Bodenschatz E, Bewley GP, Nobach H, Sinhuber M, Xu H (2014) Variable density turbulence tunnel facility. Rev Scientif Instrum 85(9):093908

Cekli HE, Van de Water W (2010) Tailoring turbulence with an active grid. Exp Fluids 49(2):409–416

Cekli HE, Joosten RR, Van de Water W (2015) Stirring turbulence with turbulence. Phys Fluids 27(12):125107

ForWind (2021) ForWind center for wind energy research, generating turbulent wind fields in the large wind tunnel, https://forwind.de/en/research/infrastructures/active-grid/ (03 february 2021)

Good GH, Warhaft Z (2011) On the probability distribution function of the velocity field and its derivative in multi-scale turbulence. Phys Fluids 23(9):095106

Griffin KP, Wei NJ, Bodenschatz E, Bewley GP (2019) Control of long-range correlations in turbulence. Exp Fluids 60(4):55

Hearst RJ, Ganapathisubramani B (2017) Tailoring incoming shear and turbulence profiles for lab-scale wind turbines. Wind Energy 20(12):2021–2035

Hearst RJ, Lavoie P (2015) The effect of active grid initial conditions on high Reynolds number turbulence. Exp Fluids 56(10):185

IEC (2019) Wind turbine generator systems, part 1 – safety requirements. Standard IEC 61400-1:2019, International Electrotechnical Commission, Geneva, Switzerland

Knebel P, Kittel A, Peinke J (2011) Atmospheric wind field conditions generated by active grids. Exp Fluids 51(2):471–481

Kolmogorov AN (1941) The local structure of turbulence in incompressible viscous fluid for very large Reynolds numbers. Cr Acad Sci URSS 30:299–303

Kröger L, Frederik J, van Wingerden JW, Peinke J, Hölling M (2018a) Generation of user defined turbulent inflow conditions by an active grid for validation experiments. J Phys: Conf Ser 1037(5):052002

Kröger L, Neuhaus L, Peinke J, Gülker G, Hölling M (2018b) Turbulence generation by active grids. In: iTi Conference on Turbulence, Springer, pp 191–196

Larssen JV, Devenport WJ (2011) On the generation of large-scale homogeneous turbulence. Exp Fluids 50(5):1207–1223

Makita H (1991) Realization of a large-scale turbulence field in a small wind tunnel. Fluid Dyn Res 8(1–4):53

Mydlarski L (2017) A turbulent quarter century of active grids: from Makita (1991) to the present. Fluid Dyn Res 49(6):061401

Mydlarski L, Warhaft Z (1996) On the onset of high-Reynolds-number grid-generated wind tunnel turbulence. J Fluid Mech 320:331–368

Mydlarski L, Warhaft Z (1998) Passive scalar statistics in high-Péclet-number grid turbulence. J Fluid Mech 358:135–175

Neuhaus L, Hölling M, Bos WJT, Peinke J (2020) Generation of atmospheric turbulence with unprecedentedly large Reynolds number in a wind tunnel. Phys Rev Lett 125(15):154503

Neunaber I, Braud C (2020) First characterization of a new perturbation system for gust generation: the chopper. Wind Energy Sci 5(2):759–773

Petrović V, Berger F, Neuhaus L, Hölling M, Kühn M (2019) Wind tunnel setup for experimental validation of wind turbine control concepts under tailor-made reproducible wind conditions. In: Journal of Physics: Conference Series, IOP Publishing, vol 1222, p 012013

Poorte R, Biesheuvel A (2002) Experiments on the motion of gas bubbles in turbulence generated by an active grid. J Fluid Mech 461:127–154

Reinke N, Homeyer T, Hölling M, Peinke J (2017) Flow modulation by an active grid. arXiv preprint arXiv:170300721

Shen X, Warhaft Z (2000) The anisotropy of the small scale structure in high Reynolds number ($R_\lambda \sim 1000$) turbulent shear flow. Phys Fluids 12(11):2976–2989

Shirzadeh K, Hangan H, Crawford C (2020) Experimental and numerical simulation of extreme operational conditions for horizontal axis wind turbines based on the IEC standard. Wind Energy Sci 5(4):1755–1770

Simmons L, Salter C (1934) Experimental investigation and analysis of the velocity variations in turbulent flow. Proc R Soc London Ser A, Contain Papers Math Phys Charact 145(854):212–234

Sinner M, Petrović V, Langidis A, Neuhaus L, Hölling M, Kühn M, Pao LY (2021) Experimental testing of a preview-enabled model predictive controller for blade pitch control of wind turbines. IEEE Transactions on Control Systems Technology pp 1–15, https://doi.org/10.1109/TCST.2021.3070342

Weitemeyer S, Reinke N, Peinke J, Hölling M (2013) Multi-scale generation of turbulence with fractal grids and an active grid. Fluid Dyn Res 45(6):061407